

CHEMISTRY IN A FORMING PROTOPLANETARY DISK: MAIN ACCRETION PHASE

Haruaki Yoneda

Department of Planetology, Kobe University, Kobe 657-8501, Japan

Yusuke Tsukamoto

Riken, 2-1 Hirosawa, Wako, Saitama, Japan

Kenji Furuya

Center for Computational Sciences, University of Tsukuba, Japan

and

Yuri Aikawa

Center for Computational Sciences, University of Tsukuba, Japan

`aikawa@ccs.tsukuba.ac.jp`

ABSTRACT

We investigate the chemistry in a radiation-hydrodynamics model of star-forming core which evolves from a cold (~ 10 K) prestellar core to the main accretion phase in $\sim 10^5$ yr. A rotationally-supported gravitationally unstable disk is formed around a protostar. We extract the temporal variation of physical parameters in $\sim 1.5 \times 10^3$ SPH particles which end up in the disk, and perform post-processing calculations of the gas-grain chemistry adopting a three-phase model. Inside the disk, the SPH particles migrate both inward and outward. Since a significant fraction of volatiles such as CO can be trapped in the water-dominant ice in the three-phase model, the ice mantle composition depends not only on the current position in the disk but also on whether the dust grain has ever experienced higher temperatures than the water sublimation temperature. Stable molecules such as H₂O, CH₄, NH₃ and CH₃OH are already abundant at the onset of gravitational collapse and simply sublimated as the fluid parcels migrate inside the water snow line. On the other hand, various molecules such as carbon chains and complex organic molecules (COMs) are formed in the disk. COMs abundance sensitively depends on the outcomes of photodissociation and

diffusion rates of photofragments in bulk ice mantle. As for S-bearing species, H₂S ice is abundant in the collapse phase. In the warm regions in the disk, H₂S is sublimated to be destroyed, while SO, H₂CS, OCS and SO₂ become abundant.

Subject headings: astrochemistry — star-formation — protoplanetary disks

1. INTRODUCTION

Stars are formed by gravitational collapse of dense cloud cores. Theoretically, this process is divided into two phases: early collapse phase and main accretion phase. The former starts from the gravitational instability of a cold starless core. Efficient cooling by dust continuum keeps the collapsing core cold. Eventually, the contraction heating overwhelms the cooling. The enhanced pressure gradient halts the collapse in the central region to form the first hydrostatic core. Dissociation of H₂ triggers the collapse of the central region of the first core, which evolves to a protostar when the dissociation and ionization of gas are completed. The initial mass of a protostar is predicted to be as small as Jovian mass (Larson 1969; Masunaga and Inutsuka 2000; Machida et al. 2010). Then the protostar acquires mass mostly from the infalling envelope in the main accretion phase. Observationally, the protostellar cores, especially those as young as Class 0, correspond to the main accretion phase. Although these star-formation processes would be common among high-mass and low-mass stars, we concentrate on low-mass stars, which are relevant to planetary system formation, in the present work.

Protostellar cores harbor rich chemistry (van Dishoeck et al. 1995; Ceccarelli et al. 2007). The low-mass protostellar cores with emission lines of complex organic molecules (COMs) are called hot corinos. A single-dish line survey towards a prototypical hot corino source, IRAS 16293-2422, has detected more than 70 species, including COMs such as CH₃CHO and HCOOCH₃ (Caux et al. 2011). Furthermore, recent ALMA observations detected glycolaldehyde, methyl formate, acetic acid and ethylene glycol towards this source (Jorgensen et al. 2012, 2016). Glycolaldehyde and ethylene glycol are also detected towards NGC1333-IRAS2A (Coutens et al. 2015; Maury et al. 2014). Maury et al. (2014) observed COMs towards NGC 1333-IRAS2A to find out that the emission lines originate from a region of radius 40-100 AU centered on the protostar. More recently, Taquet et al. (2015) performed interferometric observations of NGC1333 IRAS 2A and IRAS 4A. They also confirmed that most of the COMs emission originates in the central ($\sim 2''$) region of the core, and derived the abundances of COMs to be $\sim 10^{-10} - 10^{-8}$ relative to hydrogen. L1527 and IRAS 15398-3359, on the other hand, are characterized by warm carbon chain chemistry (WCCC) (Sakai et al. 2008, 2009).

Both COMs and carbon-chains are considered to be formed by combination of gas-phase and grain-surface reactions (Herbst & van Dishoeck 2009). Garrod & Herbst (2006) calculated gas-grain chemistry assuming a constant density and increasing temperature to mimic the heating via star-formation. They found that icy radicals, which are largely produced by cosmic ray-induced photodissociation, start to migrate on grain surfaces to form COMs at several tens of K, and that the gas-phase reactions are strongly coupled to this process as well. Aikawa et al. (2008) and Aikawa et al. (2012) then adopted the chemical reaction network of Garrod & Herbst (2006) to the 1D (spherical symmetric) radiation hydrodynamics model of low-mass star formation (Masunaga et al. 1998; Masunaga and Inutsuka 2000). They investigated spatial distributions of molecular abundances and their dependencies on the evolutionary stage of the core. They also confirmed that carbon chains are formed at luke-warm temperatures triggered by the sublimation of methane, as suggested by Sakai et al. (2008). A recent statistical survey indicates that carbon chains and COMs indeed coexist in some protostellar cores (Graninger et al. 2016; Imai et al. submitted).

At the center of a core, a protostar (or protostars) and disk system are formed. Thus COMs and carbon chains may eventually be incorporated into the disk. A recent ALMA observation indicates that COMs are associated with disk-forming region, at least in the case of IRAS 16293 (Oya et al. 2016). Theoretical models of Class II disks, on the other hand, show that chemistry in the disk midplane would not be efficient enough to significantly change the abundances and hydrogen isotope ratios of stable icy molecules, especially if the cosmic-ray ionization is prohibited by stellar winds and/or magnetic fields (Aikawa et al. 1999; Cleeves et al. 2014), although the gas-phase chemistry is active in the disk surface and warm molecular layers (Dutrey et al. 1997; Aikawa et al. 2002; Qi et al. 2011; Rosenfeld et al. 2013; Henning & Semenov 2013). Thus chemistry in protostellar cores and forming disks could play an important role in determining the raw material of planetary systems.

Disk formation processes, in turn, could affect the molecular evolution in the central region of the protostellar core. Theoretical models have predicted that COMs are efficiently formed at several tens of K. If the collapse is spherical (i.e. no rotation and thus without disk), gas and dust in the envelope fall onto the protostar in the free-fall timescale. Then COMs formation in the infalling material is limited by the short timescale for them to go through the luke-warm regions ($\lesssim 10^3$ AU) of the envelope. If the gas and dust are incorporated into the disk, COMs formation could proceed in the disk for a longer timescale. Chemistry in forming disks has been studied by several groups. Furuya et al. (2012) and Hincelin et al. (2013) adopted the results of 3-D (magneto-) radiation hydrodynamics models (Tomida et al. 2010; Commerçon et al. 2011) to calculate molecular evolution from a prestellar core to the first hydrostatic core, which is the precursor of a protoplanetary disk. They found that the first core harbors COMs, although their abundances are yet limited due to the short lifetime

(\lesssim a few 10^3 yr) of the first core and more compact luke-warm regions than those in the protostellar stage. Visser et al. (2009, 2011) constructed a two-dimensional semi-analytical model of disk formation, starting from the singular isothermal sphere. Although the model proceeds to the protostar phase (i.e. beyond the first core), their grain-surface chemistry is limited to rather simple reactions such as hydrogenation. Evolution of complex organic molecules in the semi-analytical model was recently investigated by Drozdovskaya et al. (2016). They showed that COMs abundance can be comparable to that of CH_3OH in the disk midplane, when all the envelope gas has accreted onto the disk.

The present work is an update from Aikawa et al. (2008) and Furuya et al. (2012); we investigate the molecular evolution from a molecular cloud core to a forming disk around a protostar (i.e. beyond the first core) with an updated chemical model. We adopt the 3-D radiation hydrodynamics (RHD) simulation of Tsukamoto et al. (2015). Full radiation hydrodynamics calculation after the first core is very time consuming, because of the extremely short time step required to calculate the structure and evolution of a protostar (Tomida et al. 2013). Tsukamoto et al. (2015) circumvent this problem by introducing a sink particle at the protostar position to successfully calculate the evolution up to 10^4 yr after the formation of the protostar. We solve the rate equations of gas-grain chemistry along the stream lines of fluid parcels, which are traced in the RHD (e.g. Aikawa 2013). Since the fluid parcels spend longer time in warm disk regions, we can expect more significant chemical evolution than in the first core stage. While the chemical network model used in this work is basically the same as that used in Aikawa et al. (2008) and Furuya et al. (2012), we adopt the three-phase model rather than the two-phase model.

The rest of this paper is organized as follows. The physical and chemical models are described in §2. The results of our fiducial model are presented in §3. In §4, we compare our fiducial model with the two-phase model, and investigate dependences of our results on some uncertain chemical parameters. We briefly compare our results with recent models and observations of forming disks. Finally, we summarize our conclusions in §5.

2. MODELS

2.1. Disk Formation

We adopt our disk formation model from a 3D radiation hydrodynamical simulation by Tsukamoto et al. (2015). The simulation starts from an isothermal, uniform and rigidly rotating molecular cloud core with mass of $1 M_\odot$ and temperature of $T = 10$ K. Tsukamoto et al. (2015) investigated models with various initial angular velocity and central density to de-

rive the criterion for disk fragmentation. We adopt the model in which a relatively massive ($> 0.2M_{\odot}$) disk is formed; angular velocity of rigid rotation, density, and core radius at the initial conditions are $\Omega = 7.61 \times 10^{-14} \text{ s}^{-1}$, $\rho = 6.91 \times 10^{-19} \text{ g cm}^{-3}$, and $r = 5.8 \times 10^3 \text{ AU}$, respectively. The gravitation collapse of the rotating core is calculated by the three-dimensional smoothed particle radiation hydrodynamics (SPRHD) code, which can treat the heating by the gas dynamics and radiative heating/cooling. We used the sink particle and does not include radiative feedback from the sink particle. Thus, it may underestimate the temperature in the disk and in falling envelope after the protostar is formed.

Figure 1 shows the distribution of column density and density-weighted gas temperature ($\int \rho T dz / \int \rho dz$) at assorted time steps at the core center on $x - y$ plane, which is perpendicular to the rotation axis. At the time of $t = t_{\text{SC}} = 9.046 \times 10^4 \text{ yr}$, the central density reaches $\sim 4 \times 10^{-8} \text{ g cm}^{-3}$. Then the gas inside the radius of 2 AU is replaced by a sink particle, which represents a protostar. The simulation continues up to $t = t_f = 1.011 \times 10^5 \text{ yr}$, when the masses of the protostar and the disk are $0.107 M_{\odot}$ and $0.221 M_{\odot}$, respectively. Here, the disk is defined as the rotationally-supported region; i.e. the centrifugal force is larger than a half of the gravitation force towards the center. Since the disk is more massive than the protostar, the rotation curve is shallower ($\Omega \propto r^{-1.1}$) than the Keplerian law ($\Omega \propto r^{-1.5}$), and the spiral arms are formed by the gravitational instability.

Among the 5.2×10^5 SPH particles used in the RHD simulation, we extract about 1.5×10^3 particles, which reside near the disk midplane at t_f , to calculate the chemical rate equations along their trajectories, i.e. taking into account the temporal variation of the gas density, temperature and UV radiation. The visual extinction A_v is used to calculate the attenuation of the interstellar UV radiation (e.g. Furuya et al. 2012). We evaluate the visual extinction of each SPH particle by calculating the column densities of interstellar matter from the particle position to the boundaries of the computational domain along the x , y and z axes in both the positive and negative directions. The minimum column density among the 6 directions is converted to the visual extinction via the formula

$$A_v = \frac{f_{\text{H}} \Sigma}{\mu m_{\text{H}}} \times 5.34 \times 10^{-22} \text{ cm}^2, \quad (1)$$

where f_{H} is the mean number of hydrogen nuclei per species (1.67), μ is the mean molecular weight (2.3) and m_{H} is the mass of a hydrogen atom (Bohlin, Savage & Drake 1978; Cardelli, Clayton & Mathis 1989). Since we adopt the SPH particles which end up in the disk midplane, A_v is mostly high ($\gtrsim 3 \text{ mag}$) so that the photodesorption and photodissociation by interstellar radiation field are not important in our model. UV radiation from the protostar is not taken into account (see discussion in §4.4). The cosmic-ray induced UV radiation, however, is ubiquitous unless the column density is much higher than 96 g cm^{-2} (see §2.2).

Figure 2 shows the distribution of extracted SPH particles color-coded according to their gas density n_{H} (panel a), temperature (b), visual extinction (c) and cosmic-ray ionization rate (d). While the density distribution shows the spiral structure due to the gravitational instability, the temperature distribution is rather axisymmetric; the heating by the spiral arm is weak and transient, and does not significantly contribute to the temperature distribution (Tsukamoto et al. 2015).

2.2. Chemical Model

Our chemical network model is basically the same as in Furuya et al. (2012). The gas-phase reactions and their rates are adopted from Garrod & Herbst (2006) at low temperatures ($T \leq 100$ K), while they are adopted from Harada, Herbst & Wakelam (2010) at higher temperatures. Reaction rate coefficients are updated following recent references; major updates include nitrogen chemistry (Wakelam et al. 2013, arXiv:1310.4350) and branching ratios of dissociative recombination of COM ions (e.g. Geppert et al. 2006; Garrod 2008). Three-body reactions and collisional dissociation reactions are included in our model; they could be effective in the central regions with high density ($\gtrsim 10^{12}$ cm $^{-3}$) and high temperature (\gtrsim several 100 K) (Furuya et al. 2012). The ionization rate is set to be

$$\zeta_{\text{eff}} = 5 \times 10^{-17} \exp \left\{ -\frac{\Sigma}{96 \text{gcm}^{-2}} \right\} + 1 \times 10^{-18} \text{s}^{-1}. \quad (2)$$

The first term is the ionization rate by cosmic rays and the second term represents the ionization by decay of radio-active nuclei.

The treatment of grain-surface reactions and interactions between the gas phase and grain surfaces is the same as in Furuya et al. (2015). The gas/dust mass ratio is set to be 100, and a uniform grain size of 0.1 μm is assumed. Grain-surface reactions and desorption energies of atoms and molecules are adopted from Garrod & Herbst (2006). We consider the Langmuire-Hinshelwood mechanism for grain surface reactions; i.e. the atoms and molecules on grain surfaces migrate via thermal hopping and react with each other when they meet. The diffusion energy barrier (E_b) is set to be half of the desorption energy (E_d) of each species. We adopt the modified rate (method A) of Garrod (2008), which takes into account the competition between surface processes (e.g. accretion versus diffusion) to improve the accuracy of the original rate equation method when the number of reactants is small on a grain surface. We take into account the competition between the reaction and diffusion out of a binding site on grain surfaces. The competition effectively enhances the probability to overcome the activation barrier, when the diffusion timescale is larger than the timescale to overcome the activation barrier. It should be noted that the activation

barrier could be overcome by tunneling, while the diffusion is assumed to be thermal in our model. We also take into account three non-thermal desorption processes: photodesorption, stochastic heating by cosmic-rays, and reactive desorption (e.g. Oberg et al. 2009a; Hasegawa & Herbst 1993; Garrod et al. 2007). The yield of photodesorption per incident photon is set to be 10^{-3} . The efficiency of reactive desorption is $10^{-3} - 10^{-2}$ per reaction for most species; it is lower for products with more vibrational modes.

In dense cold cores, ice mantles become thicker than a monolayer. Then the question is if the diffusion (hopping) rate is the same on the surface and in deeper layers. It is intuitive to expect that diffusion would be less efficient in deeper layers, if the ice mantle is dense. In fact, laboratory experiments show that hydrogen atoms adsorbed onto ice mantle can penetrate and react with only the several surface monolayers (Fuchs et al. 2009; Ioppolo et al. 2010). There are, however, other experiments that suggest diffusion of molecules in bulk ice. Oberg et al. (2009c), for example, found that the water ice mixture containing either CO_2 or CO , segregate through surface diffusion and bulk diffusion. The effective diffusion rate in the deep layers would depend on the structure of the ice mantle, e.g. cracks and porosity. Thus we calculate two models: the two-phase model and the three-phase model. The former corresponds to the case with very efficient bulk diffusion, while the latter corresponds to the other extreme, i.e. no bulk diffusion. We adopt the three-phase model as our fiducial model and compare the two models in discussion (§4.1).

The two-phase model consists of gas phase and ice phase (i.e. grain surface species). All icy molecules and atoms are assumed to migrate via thermal hopping and to be chemically active. In the three-phase model, ice phase is divided to surface layers and inner bulk (Hasegawa & Herbst 1993; Garrod & Pauly 2011). Only the surface layers, which is set to be 4 monolayers in the present work, are subject to diffusion, reaction and desorption. Both in the two-phase and three-phase models, we assume that only the top 4 monolayers are subject to photodissociation, and calculate their rates accordingly (Furuya et al. 2015). In other words, although the UV radiation can penetrate into the deeper layers of ice mantle, we assume that photofragments recombine immediately to reform their mother molecules rather than migrate and form new molecules. The dependence of molecular evolution on this assumption is discussed in §4.2.

We assume the so-called low-metal elemental abundance (Table 2 of Furuya et al. 2012). The molecular abundances at the onset of gravitational collapse are set by calculating a molecular evolution with the three-phase model for 1×10^6 yr under cloud core conditions: the temperature of $T = 10$ K, the density of $n_{\text{H}} = 2 \times 10^4 \text{ cm}^{-3}$, the visual extinction $A_{\text{v}} = 10$ mag, and the cosmic-ray ionization rate $\zeta_{\text{CR}} = 5 \times 10^{-17} \text{ s}^{-1}$ (Dalgarno 2006).

3. RESULTS

Figure 3 shows the frequency distribution of the total (gas and ice) abundances of the most abundant molecules at $t = t_f$ for (a) C-bearing, (b) N-bearing, (c) O-bearing and (d) S-bearing species in the $\sim 1.5 \times 10^3$ SPH particles. The color indicates the number of SPH particles with the specific molecular abundance; it is thick green, if the number of SPH particles is 20 or larger. The initial abundances are denoted by the star symbols. While the major stable molecules, such as CO and H₂O, keep their initial abundances, less abundant molecules with the initial abundance of $\lesssim 10^{-5}$ tend to evolve significantly during the simulation. In order to understand when and how these molecules are processed, we pick up one SPH particle and describe its physical and chemical evolution in the following subsection.

3.1. Molecular Evolution in a SPH particle

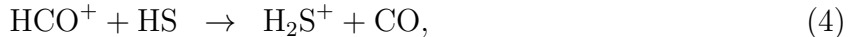
Figure 4 shows the trajectory (a-c) and the temporal variation of density and temperature (d-e) of a SPH particle, which was initially at the radius of 2.5×10^3 AU. At $\sim 8.6 \times 10^4$ yr, the SPH particle falls onto the forming disk, and starts to rotate around the first core. Figure 4 (c) and (e) shows the trajectory and physical parameters of the SPH particle after entering the disk. While the disk is rotationally supported, the trajectory is fluctuated by the dynamical effect such as the spiral arm, which results in the temporal variation of the temperature and density. At $t = t_{SC}$ (i.e. 9.046×10^4 yr), the central region of the first core collapses to form the protostar, while the rotationally-supported outer regions become the circumstellar disk.

3.1.1. infalling phase

Temporal variation of molecular abundances in the SPH particle is shown in Figure 5. The left column shows the evolution in the infalling phase, $t \leq 8.65 \times 10^4$ yr, in which the density gradually increases, while the temperature remains almost constant ~ 10 K. As the density rises, gaseous molecules are depleted onto grains. The major icy molecules, CO, CH₃OH, H₂CO, and CH₄ among C-bearing species, H₂O among O-bearing species, and NH₃ among N-bearing species, are abundantly formed before the onset of collapse.

Among S-bearing species, atomic sulfur is the most abundant at the onset of gravita-

tional collapse. It is converted to HS and H₂S by the following gas-phase reactions,



and a series of hydrogenation on grain surfaces



On the grain surface, H₂S can be converted back to HS via $\text{H}_{\text{ice}} + \text{H}_2\text{S}_{\text{ice}} \rightarrow \text{H}_{2\text{ice}} + \text{HS}_{\text{ice}}$. Although this reaction has an activation barrier of 860 K, it proceeds as efficiently as the hydrogenation of HS, due to the competition between the reaction and H atom diffusion. The abundances of HS and H₂S ices are thus similar (Furuya et al. 2015). SO is formed in the gas phase via $\text{S} + \text{OH} \rightarrow \text{SO} + \text{H}$, and on grain surfaces via $\text{HS}_{\text{ice}} + \text{O}_{\text{ice}} \rightarrow \text{SO}_{\text{ice}} + \text{H}_{\text{ice}}$.

3.1.2. forming disk

The right column of Figure 5 shows the molecular evolution after the SPH particle entered the forming disk. Both density and temperature fluctuate in a very short timescale, \sim a few hundred years. Molecular abundances are more sensitive to temperature than to density. For example, at the time of $\sim 9.4 \times 10^4$ yr, the temperature rises from ~ 50 K to ~ 150 K, as the SPH particle migrates inwards. Then the major icy molecules, such as CO, CH₄, and H₂S, sublime to the gas phase. Although the sublimation temperature of these molecules are much lower than 150 K, they have been trapped in water-dominant ice mantle, which is characteristic of the three-phase model (e.g. Vasyunin & Herscht 2013a), and is often observed in sublimation of mixed ice in the laboratory (e.g. Collings et al. 2004).

CO, CH₄, H₂O, NH₃, and CH₃OH remain abundant in the gas phase after sublimation in our model, partly because we follow the evolution only for $\sim 10^4$ yrs after the sublimation. Astrochemical models of hot cores (e.g. Charnley, Tielens & Millar 1992; Millar & Hatchell 1998) and T Tauri disks (Nomura et al. 2009) show that CH₄, NH₃ and CH₃OH are destroyed by the gas-phase reactions in $10^4 - 10^5$ yr after sublimation. This timescale is not sensitive to the gas density, because the main reactants are ions, as long as the ionization rate is $\sim 10^{-17} \text{ s}^{-1}$ and the temperature is \lesssim a few 100 K. On the other hand, H₂S, which

also forms abundantly in the envelope, is destroyed by the reaction with atomic hydrogen (see below) (Millar & Hatchell 1998).

The abundances of complex organic molecules such as HCOOH¹, HCOOCH₃ and CH₃OCH₃ increase in the disk. They can form by both gas-phase and grain-surface reactions. In the gas-phase, HCOOH forms mainly by OH + H₂CO (see discussion in §4.3). HCOOCH₃ forms by H₃CO⁺ + H₂CO → H₂COHOCH₂⁺ and subsequent dissociative recombination. CH₃OCH₃ forms by H₃CO⁺ + CH₄ → CH₃OCH₄⁺ and subsequent recombination. This protonated ion can also form by CH₃⁺ + CH₃OH, once the SPH particle migrates inside the CH₃OH snowline. Due to the high gas density ($\sim 10^{11}$ cm⁻³), these gas-phase products are promptly adsorbed onto grains at $T \lesssim 150$ K. On grain surfaces, HCOOH forms by OH_{ice} + HCO_{ice}, and HCOOCH₃ forms by HCO_{ice} + CH₂OH_{ice}, while CH₃OCH₃ forms by CH_{3ice} + CH₂OH_{ice}. It should be noted that CH₂OH and CH₃O are not discriminated in our model.

Carbon chains also form in the disk. Once the gaseous methane becomes relatively abundant ($\sim 5 \times 10^{-7}$) at 8.8×10^4 yr, it reacts with C⁺ to produce C₂H₃⁺ or C₂H₂⁺. The latter reacts with H₂ to form C₂H₄⁺. Then C₂H₄⁺ and C₂H₃⁺ dissociatively recombine with electron on grain surfaces to form acetylene, C₂H₂. C₂H₆ forms by successive hydrogenation of C₂H₂ on grain surfaces. In the later stage ($\gtrsim 9.8 \times 10^4$ yr), C₂H₂ also forms by CH₂ + CH₂ → C₂H₂ + H + H in the gas phase. C₃H₂ and C₄H, which are thought to characterize the WCCC sources such as L1527, are not abundant in the forming disk due to the high density and high temperature (Aikawa et al. 2012). C₃H₂ is protonated, and C₄H is transformed to C₄H₂ via the gas-phase reaction with H₂.

While the abundances of H₂S and HS are almost the same in the envelope, the partial sublimation of HS starts earlier than that of H₂S due to higher volatility. Then HS reacts with atomic H to form atomic S, or reacts with atomic S to form S₂. The sublimation of major S-bearing ices at $\sim 9.4 \times 10^4$ yr triggers active gas-phase chemistry. H₂S is destroyed by H₂S + H → HS + H₂; although this reaction has an activation barrier of 1350 K, the warm temperature (> 70 K) helps to overcome the barrier. Then SO and H₂CS form by O + S₂ and S + CH₃, respectively (Charnley 1997). CS forms by CH₂ + S. After the water ice sublimates into the gas phase together with the entrapped minor ices ($t \gtrsim 9.8 \times 10^4$ yr), SO₂ and OCS form by OH + SO, and S + CO, respectively. Since the proton affinity of OCS is higher than that of CO but lower than that of H₂O, destruction of OCS via protonation, i.e. OCS + HCO⁺ → HOCS⁺ + CO, becomes inefficient, after the water sublimation.

It should be noted that at warm temperatures (\gtrsim a few 10 K), H₂ formation on ice mantle

¹Although HCOOH is made of only five atoms, we count it as COMs, because it is characteristic of hot corinos.

surfaces is inefficient. Then H atom, which is the major reactant of HS and H₂S, becomes as abundant as $10^{-7} - 10^{-6}$ relative to hydrogen (i.e. $n(\text{H}) \sim 10^5 - 10^6 \text{ cm}^{-3}$). At $T > 100$ K, we assume the efficient H₂ formation via chemisorption site (Cazaux & Tielens 2004), which lowers the H atom abundance temporally. Duration time of such high temperature is, however, rather limited, and the H₂S abundance significantly decreases before the fluid parcel reaches the innermost hot region of the disk.

3.2. Cloud Origin or Disk Origin

In the astrochemical studies of protoplanetary disks, it is often argued how much fraction of disk material inherits the chemical composition of ISM, and how much fraction is chemically reset in the disk. Based on our simulation, here we discuss which molecule originates in the cloud (i.e. inherit from ISM) and which forms in the young disk (i.e. reset). Figure 3 shows that chemical composition in the forming disk is quite different from our initial condition, which is set by calculating the molecular evolution for 1×10^6 yr under the cloud core conditions. In the previous subsection, however, we have seen that the molecular evolution proceeds not only in the disk, but also in the cold infalling phase. For example, the abundance of H₂S increases, while that of C₂H₂ decreases by orders of magnitude in the infalling phase. In the context of inherit or reset, we thus divide the major molecules into two groups according to whether they are formed before entering the disk (i.e. before the onset of collapse and in the infalling envelope) or in the forming disk (Table 1). We call the former group as “Cloud” for brevity. Each group is further divided into two groups, based on whether or not they are destroyed in inner regions of the disk.

Figure 6 shows the distribution of representative species at the final timestep. CO originates in a cloud before the onset of collapse, and sum of its abundance in the gas phase and ice mantle is almost constant. H₂S is abundant in the outer disk, since it is efficiently formed in the collapse phase. It is then destroyed in the gas phase after sublimation at \lesssim a few tens of AU. HCOOH and SO₂ form in the inner disk, and thus have a centrally peaked distribution.

Table 1: Formation site of molecules

formation site	species	destroyed
Cloud	CO, CH ₄ , CH ₃ OH, H ₂ O, NH ₃ , CO ₂ , H ₂ CO	HS, H ₂ S
Disk	HCOOCH ₃ , HCOOH, C ₂ H ₆ , C ₂ H ₂ CH ₃ OCH ₃ , H ₂ CS, SO ₂ , OCS	S ₂ , CS

Our assignment of formation site of molecules is qualitatively similar to the result of Hincelin et al. (2013), who investigated the molecular evolution from the collapsing core to the first core. They suggested that CH_3OH and H_2S originate in the parental cloud, while HCOOH and OCS are formed in the warm region close to the first core. But there are also significant differences between our results. Firstly, we include a chain reaction of CO_2 formation triggered by OH formation on CO ice mantle (Garrod & Pauly 2011), which makes CO_2 much more abundant than in Hincelin et al. (2013), although our value is yet lower than the observed CO_2 ice abundance in molecular clouds (Bergin et al. 2005). Secondly, many molecules, such as SO and COMs, are more abundantly produced in our model than in Hincelin et al. (2013). The longer timescale and more extended region of warm temperature in our model allow the active chemical evolution. For the same reason, the present model gives higher abundances of COMs than our previous work which focused on the first core (Furuya et al. 2012).

It should be noted that our model might underestimate the chemical evolution in the envelope, since our model does not take into account the envelope heating by protostellar irradiation. In the model of Visser et al. (2011), for example, warm temperature (\gtrsim a few tens of K) regions in the envelope extend to several 100 AU. The infalling gas and dust experience such warm temperature for a few 10^3 yrs, during which some fraction of COMs could be formed (see also Aikawa et al. 2012). Our model, however, corresponds to earlier stage than that of Visser et al. (2011), who followed the longer term evolution ($\sim 2 \times 10^5$ yr after the protostellar birth). In our model, many SPH particles are incorporated to the rotationally-supported disk before the protostar is formed. It indicates that the assignment of formation site of molecules, whether they are mainly formed in the disk or collapsing envelope, depends on the evolutionary stage of the core.

3.3. Radial Distribution

The upper panel of Figure 7 shows temperature and number density of hydrogen nuclei of $\sim 1.5 \times 10^3$ SPH particles at t_f as functions of radius. The plotted particles all exist at $|z| \leq 0.2R$, where z is distance from the midplane and R is distance from the rotation axis. Since the disk is nonaxisymmetric with the spiral structures (Figure 2), the density and temperature have a range of values at each radius. The CO abundance (Figure 7 lower panel) also shows a significant scatter especially at $R \geq 70$ AU and at $10 \text{ AU} \lesssim R \lesssim$ a few tens of AU. The scatter at the outer radius is mainly caused by the variation of physical conditions; when the CO abundance in the SPH particles is plotted as a function of temperature, the scatter becomes smaller. The scatter at the inner radii, on the other hand, is caused by radial

migration of the SPH particles. As we have seen in Figure 4, the SPH particles migrate both inwards and outwards after entering the disk. Since the dominant component of ice mantle is water, and since we adopt the three-phase model, only a fraction of CO ice is sublimated at its own sublimation temperature ~ 20 K. At the sublimation temperature of H_2O , on the other hand, the whole mantle evaporates. When a SPH particle loses its ice mantle and migrates out to $R \sim$ a few tens of AU, CO does not freeze out due to warm temperatures of $T \gtrsim 20$ K. Thus at $10 \text{ AU} \lesssim R \lesssim$ a few tens of AU, the SPH particles with high CO ice abundance ($\sim 3 \times 10^{-5}$) and low CO gas abundance coexist with those having high CO gas abundance and low CO ice abundance. This has three implications. Firstly our simulation clearly shows that the ice mantle composition keeps “memory” of the dust trajectory, so that dust particles at similar radii could have significantly different mantle composition. Secondly, the radial abundance variation over the snow line is smoothed by the outward migration of gas. Finally, our simulation shows that mixing of gaseous composition could be important, which is not taken into account in the present work and should be investigated in future work.

The solid lines in the lower panel of Figure 7 show azimuthally averaged molecular abundances as a function of radius. We constructed a circular coordinate with 532 radial grids and 100 azimuthal grids, and interpolated the density and molecular abundances at SPH particle positions to obtain the values at each grid point. Then we calculated the azimuthally averaged abundances, i.e. total number of the molecule divided by total number of hydrogen nuclei, at each radius. The averaged abundances show spiky features especially at low abundance range, reflecting the original scatter of the molecular abundances.

Figure 8 shows azimuthally averaged abundances of assorted species. The spiky features, i.e. the variations of the averaged abundance over a short radial distance, are caused by the scattered molecular abundances in radial bins, as we have seen for CO (Figure 7). Transition of icy molecules to gaseous species occur mostly at $R \sim 10$ AU, where water ice sublimates, although very volatile species such as CO and N_2 have relatively high gas-phase abundances even outside the water snow line.

4. DISCUSSION

4.1. Comparison with the Two-phase Model

In the three-phase model, we assumed no diffusion in the inert bulk layer of ice mantle, which results in a significant ($\sim 85\%$) entrapment of CO in water ice mantle. In reality, however, molecules in the bulk ice mantle could diffuse slowly. Fayolle et al. (2011) found

in the laboratory experiments of H₂O/CO₂/CO ice mixture that the fraction of CO trapped in water ice varies from 4% to 96 %, depending on the ice mantle thickness and ice composition. While they constructed a detailed rate equation model with swapping of ice mantle species to reproduce the laboratory experiments, an implementation of their formulation with extrapolations to various ice species is out of the scope of the present work. In order to investigate the dependence of molecular abundances on the bulk ice diffusion, we calculate another extreme case, the two-phase model, in which molecules in the whole ice mantle can migrate thermally.

Azimuthally averaged molecular abundances for the two-phase model are presented in Figure 9. An apparent difference between the three-phase and two-phase models is that, in the two-phase model, icy molecules are sublimated at their own sublimation temperatures. Abundances at the innermost radii, which correspond to the final abundances in the temporal variation, are similar between two-phase and three-phase models for many molecules, although there are some exceptions.

In the two-phase model, CH₃OH is slightly more abundant than CO, since the whole CO ice is subject to hydrogenation, i.e. the conversion to CH₃OH. Among COMs, HCOOCH₃ is more abundant in the two-phase model than in the three-phase model. HCOOCH₃ is formed by H₃CO⁺ + H₂CO → H₂COHOCH₂⁺ and subsequent recombination in the gas phase, and radical-radical association of HCO_{ice} + CH₂OH_{ice} on grain surfaces both in the two-phase and three-phase models. Sublimation of H₂CO at $R \sim 30$ AU enhances the gas-phase formation of HCOOCH₃ in the two-phase model. It also enhances the production of gaseous HCO, which is adsorbed onto grains to form HCOOCH₃.

C₂H₂ and C₃H₂ are sublimated at ~ 30 AU, where they are promptly destroyed by gas-phase reactions. In later stage, $t \sim 9.8 \times 10^4$ yr, the C₂H₂ and C₃H₂ abundances are determined by the gas-phase reactions to be similar to those in the three-phase model.

Major N- and O-bearing species in Figure 9 are formed mostly in the cloud before the onset of collapse and collapse phase, and are simply sublimated in the disk. Their abundances in the innermost radii are similar between the two-phase and three-phase models, as they are mostly determined by the initial abundances.

H₂S ice is the dominant S-bearing species outside $R \sim 20$ AU, and is converted to H₂CS and SO in the inner radius, as in the three-phase model. OCS in the two-phase model is slightly less abundant than in the three-phase model, reflecting the lower CO abundance, since OCS is mainly formed by CO + S. S₂ is efficiently formed via HS + S at $R \sim 40$ AU, where HS is sublimated. Then CS is formed by C + S₂.

4.2. Dependences of COM Abundances on Ice Photodissociation Rate

The previous subsection showed that COM abundances are higher in the two-phase model than in the three-phase model. The enhancement is, however, only one order of magnitude or so. The formation of COMs is actually limited by the formation of radicals via photodissociation of icy molecule, which is restricted to the top 4 monolayers in our model, assuming that the photofragments in deeper layers efficiently recombine rather than migrate and form new molecules. In this subsection, we investigate the dependence of COM abundances on this assumption by letting the whole ice mantle to be subject to photodissociation and subsequent chemical reactions in the two-phase model. The COMs formation is also expected to be enhanced if the ratio of diffusion energy barrier to desorption energy barrier is smaller (Walsh et al. 2014). We thus recalculate the temporal variation of molecular abundances in the SPH particle described in §3.1 with three different settings (Table 1). In model A, the ratio E_b/E_d is set to be 0.3, and the photodissociation of ice mantle is effective only in the top 4 monolayers. In model B and C, the whole ice mantle is subject to the photodissociation. The ratio E_b/E_d is 0.3 in Model B, while it is 0.5 in model C.

The top panels in Figure 10 show the result of Model A. Comparing the final COMs abundance with that in Figure 9, we can see that the COM abundances are enhanced by only a factor of a few.

In Model B (the middle panels in Figure 10), the abundances of HCOOCH_3 and CH_3OCH_3 are enhanced by more than an order of magnitude compared with those in Model A. Formation of these COMs are efficient even in the cold (~ 10 K) envelope, since the thermal diffusion barrier is set to be small especially for small (e.g. two-atom or three-atom) radicals. In Model C (the bottom panels), COMs formation in the cold envelope is inefficient due to the high E_b compared to Model B, while the COM abundances in the disk are higher than in Model A. We conclude that COM abundances are more sensitive to the efficiency of ice mantle photodissociation than on E_b/E_d . If the ice mantle photodissociation is efficient

Table 1: Model settings and COMs abundance

Model	phase	E_b/E_d	photodiss. ^a
A	two	0.3	4
B	two	0.3	all
C	two	0.5	all

^aNumber of ice mantle layers which are effectively subject to the photodissociation.

and E_b/E_d is low, COMs can be abundantly formed even in low temperatures.

4.3. Uncertainties of Rate Coefficients for COMs formation

In our model, the abundance of NH_2CHO is as high as $\sim 10^{-7}$ in the initial condition and remains high throughout the simulation (Figure 3). Its abundance estimated towards hot corino objects, on the other hand, is $\sim 10^{-11} - 10^{-9}$ (Lopez-Sepulcre et al. 2015). In our model NH_2CHO is formed mainly by association of $\text{CH}_2\text{OH}_{\text{ice}} + \text{N}_{\text{ice}}$ on grain surfaces. This formation pathway is more effective compared with our previous work, since we updated the photodissociation branching ratio of CH_3OH ice following Oberg et al. (2009b), who suggested that $\text{CH}_2\text{OH} + \text{H}$ is the major branch based on the laboratory experiment. The association reaction, however, may not lead to NH_2CHO , since the re-arrangement of chemical bonds is required.

HCOOH forms mainly by $\text{OH} + \text{H}_2\text{CO}$ in the gas phase, and $\text{OH}_{\text{ice}} + \text{HCO}_{\text{ice}}$ on grain surfaces in our model. The rate coefficient of the former gas-phase reaction is set to be $2.01 \times 10^{-13} \text{ cm}^3 \text{ s}^{-1}$ in our model. Xu et al. (2006), however, found that the association of $\text{OH} + \text{H}_2\text{CO}$ has an activation barrier of 2156 K. We may have overestimated the formation rate of HCOOH in the gas phase.

In order to check the effect of these reactions in our model, we recalculate the molecular evolution in the SPH particle described in §3.1, setting the initial NH_2CHO ice abundance to be zero and turning off the reactions $\text{CH}_2\text{OH}_{\text{ice}} + \text{N}_{\text{ice}} \rightarrow \text{NH}_2\text{CHO}_{\text{ice}}$ on the grain surface and $\text{OH} + \text{H}_2\text{CO} \rightarrow \text{HCOOH} + \text{H}$ in the gas phase. The HCOOH abundance in the final timestep is reduced to 7×10^{-11} , but NH_2CHO is as abundant as 1×10^{-7} relative to hydrogen nuclei. The latter is mainly formed by the gas-phase reaction of $\text{NH}_2 + \text{H}_2\text{CO}$, the rate coefficient of which is adopted from the ab-initio calculation by Barone et al. (2015).

It should also be noted that several groups proposed new gas-phase formation pathways of COMs, which are not included in our model (Vasyunin & Herbst 2013b; Balucani et al. 2015; Taquet et al. 2016). Although these new reactions were introduced to account for gaseous COMs observed in prestellar cores (Bacmann et al. 2012; Vastel et al. 2014), they could be effective in the warm regions of forming disk as well.

4.4. Comparison with the Previous Models and Observations

Chemistry in gravitationally unstable disk is previously investigate by Ilee et al. (2011) and Evans et al. (2015). They showed that icy molecules are desorbed to the gas phase by

the shock heating at the spiral arms. Our model shows a similar feature, although the enhancement of temperature and gas-phase molecular abundances at the spiral arms is less prominent than in Evans et al. (2015) (§2.1). Comparing Figure 2 (b) and Figure 6 we can see that the gas-phase molecules are abundant in the warm temperature ($T \gtrsim 100$ K) region, which is tilted by the spiral arms. Since the gas density is higher by a factor of a few at the spiral arms than the inter-arm region, the spiral structure would become more apparent in the distribution of gaseous molecular column densities than in the abundance distribution shown in Figure 6. Evans et al. (2015) also showed that the spiral arms are well traced by CN and that CO, SO, OCS, NH₃, H₂O and H₂S are significantly affected only by the adsorption and desorption. In our model, on the other hand, CN is not abundant due to its high chemical reactivity and lower sublimation temperature (~ 40 K) than assumed in Evans et al. (2015). While the total (gas and ice) abundances of CO, NH₃, and H₂O remain almost constant in our model, S-bearing species are subject to active chemistry in the gas-phase. It is not clear why the S-chemistry is different between our model and Evans et al. (2015). The reactions of S-bearing species described in §3.1.2 are included in UMIST95, which is adopted in Evans et al. (2015). Possible causes could be a short duration (2047 yr) of the chemical calculation and initial abundances in Evans et al. (2015). Their initial abundance is set referring to cometary ice abundance, rather than calculating the molecular evolution in the molecular clouds and/or collapsing core; SO and OCS are relatively abundant ($\sim 10^{-6}$), while H atom and O atom are absent.

Drozdovskaya et al. (2016) investigated COMs formation in the semi-analytical disk formation model of Visser et al. (2009). They found that COM abundances can be comparable to that of CH₃OH in the disk midplane, when all the envelope gas has accreted onto the disk. Although there are many differences between our chemical and physical models, the major differences would be twofold. Firstly, they investigate the disk composition at the end of the envelope accretion, considering the stellar UV radiation and the outflow cavity. The infalling material is thus significantly irradiated by stellar UV, which triggers the COMs formation by producing radicals in ice mantle. It indicates that the molecular abundance in the envelope and disk would change as the envelope mass decrease (Furuya et al. 2016). Secondly, their ice mantle chemistry is similar to our Model B in section §4.2; which is the most optimistic model for COMs formation among our models.

While various COMs have been observed in hot corino sources, derivation of their abundance relative to hydrogen is not straightforward, because non-spherical small-scale ($\lesssim 100$ AU) structures, together with the line opacities and excitation conditions, need to be considered (e.g. Visser et al. 2013). Taquet et al. (2015) observed NGC 1333-IRAS 2A and -IRAS 4A with the Plateau de Bure interferometer and detected multiple lines of COMs coming mostly from the central compact region ($\lesssim 0.2 - 0.36$ arcsec). The COMs abun-

dances derived by Taquet et al. (2015) are $4 \times 10^{-9} - 1 \times 10^{-8}$ for CH_3OCH_3 , $(1 - 2) \times 10^{-8}$ for HCOOCH_3 and $4 \times 10^{-7} - 1 \times 10^{-6}$ for CH_3OH . While the abundance of CH_3OCH_3 in our fiducial model is consistent with that derived from the observation, our model overestimates the CH_3OH abundance. The HCOOCH_3 abundance of Taquet et al. (2015) is better reproduced in Model A (Figure 10) than in our fiducial model.

Observations of CO towards protostellar cores indicate that gaseous CO increases inside the radius of $T \sim 20$ K, i.e. the CO snow line, but that the abundance of sublimated CO is lower than its canonical value ($\sim 10^{-4}$) (e.g. Fuente et al. 2012; Anderl et al. 2016). Favre et al. (2013) also found that gaseous CO is depleted in the warm layer of the class II disk, TW Hya. Entrapment of CO in water ice, as observed in our three-phase model, could be an explanation for the low gaseous CO abundance at $T \gtrsim 20$ K, although there are other possibilities such as the chemical conversion of CO to less volatile species (Bergin et al. 2014; Furuya & Aikawa 2014).

Oya et al. (2016) analyzed ALMA Cycle-1 data of IRAS 16293-2422 and found that CH_3OH and HCOOCH_3 are concentrated around the inner part of the infalling-rotating envelope. They also found that H_2CS emission originates both in the envelope and the disk inside the centrifugal barrier of 40 – 60 AU. OCS, on the other hand, mainly traces the infalling-rotating envelope, although its existence in the disk component cannot be ruled out. It should be noted that our model at the final timestep is still younger and colder than IRAS 16293-2422. CH_3OH emission towards IRAS 16293-2422 indicates that the inner part of the infalling-rotating envelope is heated to $\gtrsim 100$ K, either by protostellar irradiation or accretion shock. We thus compare our model results around H_2O snow line with the observed chemical structure around the centrifugal barrier of IRAS 16293-2422. CH_3OH and HCOOCH_3 are naturally sublimated to be abundant in the gas phase inside the H_2O snow line in our model. H_2CS is abundant both in the envelope (Figure 5 left column) and inside the H_2O snow line. OCS exists in the envelope, as observed, but is also abundant inside the H_2O snow line, where HCO^+ is depleted.

5. SUMMARY

We investigated molecular evolution from a dense molecular cloud core to a forming disk in the main accretion phase. Our findings are as follows.

1. Major stable molecules such as CO, CH_4 , CH_3OH , H_2O , NH_3 and CO_2 are abundantly formed in the cloud before the onset of collapse and in collapsing phase, while COMs are mainly formed in the forming disk. Carbon chains such as C_2H_6 and C_2H_2 increase

in the warm regions in the disk, as well.

2. Among S-bearing species, H₂S is abundant in the collapse phase, but it is destroyed in the gas phase upon sublimation in the forming disk. SO, H₂CS, OCS and SO₂ become abundant in warm regions in the disk.
3. Comparisons between the present work and other recent models indicate that the molecular evolution in the infalling envelope becomes more significant as the temperature rises and density (i.e. the UV attenuation) decreases in the envelope.
4. In the three-phase model, only a fraction of volatile species, such as CO, is sublimated at their own sublimation temperatures, and the remaining fraction is trapped in water ice mantle in the warmer regions. They are fully desorbed to the gas phase at the water sublimation temperature. In the two-phase model, on the other hand, icy molecules are sublimated at their own sublimation temperatures. Nevertheless, the gas-phase abundances at the inner most radii are rather similar between the three-phase and two-phase models for many molecules.
5. The fluid parcels (i.e. the SPH particles) migrate both inward and outward in the disk. In the three-phase model, ice-coated dust grains with various ice composition, e.g. with and without CO ice, co-exist outside the water snow line.
6. COM abundances sensitively depend on the outcomes of photodissociation and diffusion of photofragments in the bulk ice mantle. Their abundances are significantly enhanced, if photofragments can migrate to form new molecules rather than simply recombine to reform its mother molecule, inside the deep ice mantle. COM abundances also increase, when a lower ratio of diffusion barrier to desorption barrier is assumed. In the model with low diffusion barrier, COMs are formed even in the cold prestellar conditions.

This work was supported by JSPS KAKENHI Grant Numbers 23540266 and 16H00931.

REFERENCES

- Aikawa, Y., Umebayashi, T., Nakano, T., & Miyama, S.M. 1999, *ApJ*, 519, 705
- Aikawa, Y., van Zadelhoff, G.J., van Dishoeck, E.F. & Herbst, E. 2002, *A&A*, 386, 622
- Aikawa, Y., Wakelam, V., Garrod, R. T., & Herbst, E. 2008, *ApJ*, 674, 993

- Aikawa, Y., Wakelam, V., Hersant, F., Garrod, R.T. & Herbst, E. 2012, *ApJ*, 760, 40
- Aikawa, Y. 2013, *ChRv*, 113, 8961
- Anderl, S., Maret, S., Cabrit, S., Belloche, A., Maury, A. J., André, Ph., Codella, C., Bacmann, A., Bontemps, S., Podio, L., Gueth, F., & Bergin, E. 2016, *A&A*, 591, A3
- Bacmann, A., Taquet, V., Faure, A., Kahane, C. & Ceccarelli, C. 2012, *A&A*, 541, L12
- Balucani, N., Ceccarelli, C., & Taquet, V. 2015, *MNRAS* 449, 16
- Barone, V., Latouche, C., Skouteris, D., Vazart, F., Balucani, N., Ceccarelli, C. & Lefloch, B. 2015, *MNRAS*, 453, L31
- Bergin, E.A., Melnick, G.J., Gerakines, P.A., Neufeld, D.A. & Whittet, C.B. 2005, *ApJ*, 627, L33
- Bergin, E.A, Cleeves, L.I., Crockett, N., Blake, G.A. 2014, *Faraday Discussion*, 168, 61
- Bohlin, R. C., Savage, B. D, & Drake, J. F. 1978, *ApJ*, 224, 132
- Cardelli, J. A., Clayton, G. C., & Mathis, J. S. 1989, *ApJ*, 345, 245
- Caux, E., kahane, C., Castets, A., Coutens, A., Ceccarelli, C., Bacmann, A., Bisschop, S., Bottinelli, S., Comito, C., Helmich, F.P., Lefloch, B., Parise, B., Schilke, P., Tielens, A.G.G.M., van Dishoeck, E.F., Vastel, C., Wakelam, V. & Walters, A. 2011, *A&A*, 532, 23
- Cazaux, S. & Tielens, A.G.G.M. 2004, *ApJ*, 604, 222
- Ceccarelli, C., Caselli, P., Herbst, E., Tielens, A. G. G. M., & Caux, E. 2007, in *Protostars and Planets V*, ed. B. Reipurth, D. Jewitt, & K. Keil (Tucson, AZ:Univ. Arizona Press), 47
- Charnley, S. B., Tielens, A. G. G. M., Millar, T. J. 1992, *ApJ*, 399, 71.
- Charnley, S.B. 1997, *ApJ*, 481, 396
- Cleeves, L.I., Bergin, E.A., Alexander, C. M.O.'D., Fujun, D., Graninger, D., Öberg, K.I., Harries, T.J. 2014, *Science*, 345, 1590
- Collings, M.P., Anderson, M.A., Chen, R., Dever, J.W., Viti, S., Williams, D.A. & McCoustra, M.R.S. 2004, *MNRAS*, 354, 1133
- Commerçon, B., Hennebelle, P. & Henning, T. 2011, *ApJ*, 742, L9

- Coutens, A., Persson, M.V., Jørgensen, J.K., Wampfler, S.F., Lykke, J.M. 2015, *A&A*, 576, A5
- Dalgarno, A. 2006, *PNAS*, 103, 33, 12269
- Drozdovskaya, M.N., Walsh, C., van Dishoeck, E.F., Furuya, K., Marboeuf, U., Thiabaud, A., Harsono, D. & Visser, R. 2016, *A&A* in press
- Dutrey, A., Guilloteau, S. & Guélin, M. 1997, *A&A* 317, L55
- Evans, M.G., Ilee, J.D., Boley, A.C., Caselli, P., Durisen, R.H., Hartquist, T.W. & Rawlings, J.M.C 2015, *MNRAS*, 453, 1147
- Favre, C., Cleaves, L.I., Bergin, E.A., Qi, C., & Blake, G.A. 2013, *ApJ*, 776, L38
- Fayolle, E.C., Öberg, K.I., Cuppen, H. M., Visser, R. & Linnartz, H. 2011, *A&A*, 529, 74
- Fuchs, G. W., Cuppen, H. M., Ioppolo, S., et al. 2009, *A&A*, 505, 629
- Fuente, A., Caselli, P., Coey, C.M., Cernicharo, J., Johnstone, D., Fich, M., van Kempen, T., van Dishoeck, E.F., Yıldız, U., Visser, R., Kristensen, L., Alonso-Alabi, T., Herpin, F. & Tisi, S. 2012, *A&A*, 540, A75
- Furuya, K., Aikawa, Y., Tmida, K., Matsumoto, T., Saigo, K., Tomisaka, K., Hersant, F. & Wakelam, V. 2012, *ApJ*, 758, 86
- Furuya, K. & Aikawa, Y. 2014, *ApJ*, 790, 97
- Furuya, K., Aikawa, Y., Hincelin, U., Hassel, G. E., Bergin, E. A., Vasyunin, A. I. & Herbst, E. 2015, *A&A*, 584, 124
- Furuya, K., Drozdovskaya, M. N., Visser, R., van Dishoeck, E. F., Walsh, C., Harsono, D., Hincelin, U., & Taquet, V., submitted to *A&A*
- Garrod, R.T. & Herbst, E. 2006, *A&A*, 457, 927
- Garrod, R.T., Wakelam, V., & Herbst, E. 2007, *A&A*, 467, 1103
- Garrod, R.T. 2008, *A&A*, 491, 239
- Garrod, R. T. & Pauly, T. 2011, *ApJ*, 735, 15
- Geppert, W. D., Hamberg, M., Thomas, R. D., Österdahl, F., Hellberg, F., Zhaunerchyk, V., Ehlerding, A., Millar, T. J., Roberts, H., Semaniak, J., Uggla, M. Af., K'allberg, A., Simonsson, A., Kaminska, M., & Larsson, M. *Faraday Discussion*, 133, 177

- Graninger, D.M., Wilkins, O.H. & Öberg, K.I. 2016, *ApJ*819, 140
- Harada, N., Herbst, R., & Wakelam, V. 2010, *ApJ*, 721, 1570
- Hasegawa, T.I. & Herbst, E. 1993, *MNRAS*, 261, 83
- Henning, T. & Semenov, D. 2013, *ChRv*, 113, 9016
- Herbst, E. & van Dishoeck E.F. 2009, *ARA&A*47, 427
- Hincelin, U., Wakelam, V., Commerçon, Hersant, F. & Guilloteau, S. 2013, *ApJ*, 775, 44
- Ilee, J.D., Boley, A.C., Caselli, P., Durisen, R.H., Hartquist, T.W. & Rawlings, J.M.C. 2011, *MNRAS*, 417, 2950
- Imai, M. et al. submitted to *ApJL*
- Ioppolo, S., Cuppen, H. M., Romanzin, C., van Dishoeck, E. F., & Linnartz, H. 2010, *Physical Chemistry Chemical Physics (Incorporating Faraday Transactions)*, 12, 12065
- Jørgensen, J. K., Cécile, F., Bisschop, S. E., Bourke, T. L., van Dishoeck, E. F. & Schmalzl, M. 2012, *ApJ*, 757, L4
- Jørgensen, J. K., van der Wiel, M.H.D, Coutens, A et al. 2016, *A&A* in press
- Larson, R.B. 1969, *MNRAS*, 145, 271
- López-Sepulcre, A., Jaber, A.A., Mendoza, M., Lefloch, B., Ceccarelli, C., Vastel, C., Bachiller, R., Cernicharo, J., Codella, A., Kahane, C., Kama, M. & Tafalla, M. 2015, *MNRAS*, 449, 2438
- Machida, M. N., Inutsuka, S. & Matsumoto, T. 2010, *ApJ*724, 1006
- Maury, A.J., Belloche, A., André, Ph., Maret, S., Gueth, F., Codella, C., Cabrit, S., Testi, L. & Bontemps, S. 2014, *A&A*, 563, L2
- Masunaga, H., Miyama, S. M., & Inutsuka, S. 1998, *ApJ*, 495, 346
- Masunaga, H., & Inutsuka, S. 2000, *ApJ*, 531, 350
- Oya, Y., Sakai, N., López-Sepulcre, A., Watanabe, Y., Ceccarelli, C., Lefloch, B. Favre, C. & Yamamoto, S. 2016, *ApJ*, 824, 88
- Millar, T.J. & Hatchell, J. 1998, *Faraday Discussions*, 109, 15

- Nomura, H., Aikawa, Y., Nakagawa, Y. & Millar, T.J. 2009, *A&A*, 495, 183
- Öberg, K.I., van Dishoeck, E. F., & Linnartz, H. 2009a, *A&A*, 496, 281
- Öberg, K.I., Garrod, R. T., van Dishoeck, E. F., & Linnartz, H. 2009b, *A&A*, 504, 891
- Öberg, K.I., Fayolle, E.C. Cuppen H.M., van Dishoeck, E. & Linnartz, H. 2009c, *A&A* 505, 183
- Qi, C., D’Alessio, P., Öberg, K.I., Wilner, D.J., Hughes, A.M., Andrews, S.M. & Ayala, S. 2011, *ApJ*, 740, 84
- Rosenfeld, K.A., Andrews, S.M., Hughes, M., Wilner, D.J. & Qi, C. 2013, *ApJ*, 774, 16
- Sakai, N., Sakai, T., Hirota, T. & Yamamoto, S. 2008, *ApJ*672, 371
- Sakai, N., Sakai, T., Hirota, T., Burton, M. & Yamamoto, S. 2009, *ApJ*697, 769
- Taquet, V., López-Sepulcre, A., Ceccarelli, C., Nari, R., Kahane, C. & Charnley, S. B. 2015, *ApJ*, 804, 29
- Taquet, V., Wirström, E.S., Charnley, S. B. 2016, *ApJ*, 821, 46
- Tomida, K., Machida, M.N., Saigo, K., Tomisaka, K. & Matsumoto, T. 2010, *ApJ*725, L239
- Tomida, K., Tomisaka, K., Matsumoto, T., Hori, Y., Okuzumi, S., Machida, M.N. & Saigo, K. 2013, *ApJ*, 763, 6
- Tsukamoto, Y., Takahashi, S.Z., Machida, M.N. & Inutsuka, S. 2015, *MNRAS*, 446, 1175
- van Dishoeck, E.F., Blake, G.A., Jansen, D.J. & Groesbeck, T.D. 1995, *ApJ*, 447, 760
- Vastel. C. Ceccarelli, C., Lefloch, B., Bachiller, R. 2014, *ApJL*, 795, L2
- Vasyunin, A. & Herbst, E. 2013, *ApJ*, 762, 86
- Vasyunin, A. & Herbst, E. 2013, *ApJ*, 769, 34
- Visser, R., van Dishoeck, E.F., Doty, S.D. & Dullemond, C.P. 2009, *A&A*, 495, 881
- Visser, R., Doty, S.D. & van Dishoeck, E.F. 2011, *A&A*, 534, 132
- Visser, R., Jørgensen, J. K., Kristensen, L.E., van Dishoeck, E.F. & Bergin, E.A. 2013, *ApJ*, 769, 19

Walsh, C. Millar, T.J., Nomura, H., Herbst, E., Widicus Weaver, S., Aikawa, Y., Laas, J.C.
& Vasyunin, A.I. 2014, *A&A*, 563, A33

Xu, S., Zhu, R.S, & Lin, C. 2006, Wiley InterScience, 322

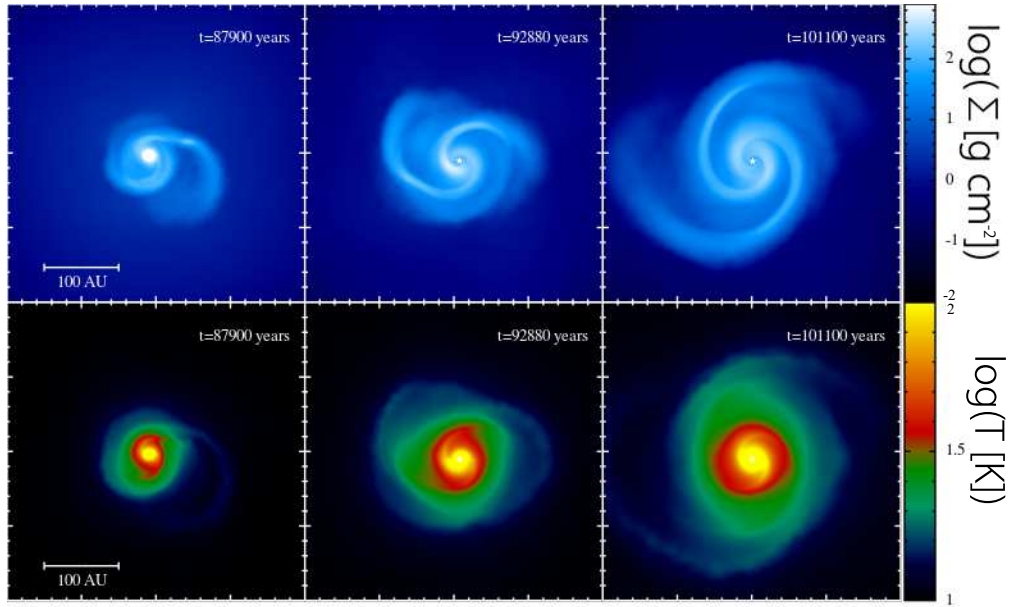


Fig. 1.— Distribution of the column density (a) and density-weighted temperature (b) viewed face-on at assorted time steps in the disk formation model by Tsukamoto et al. (2015).

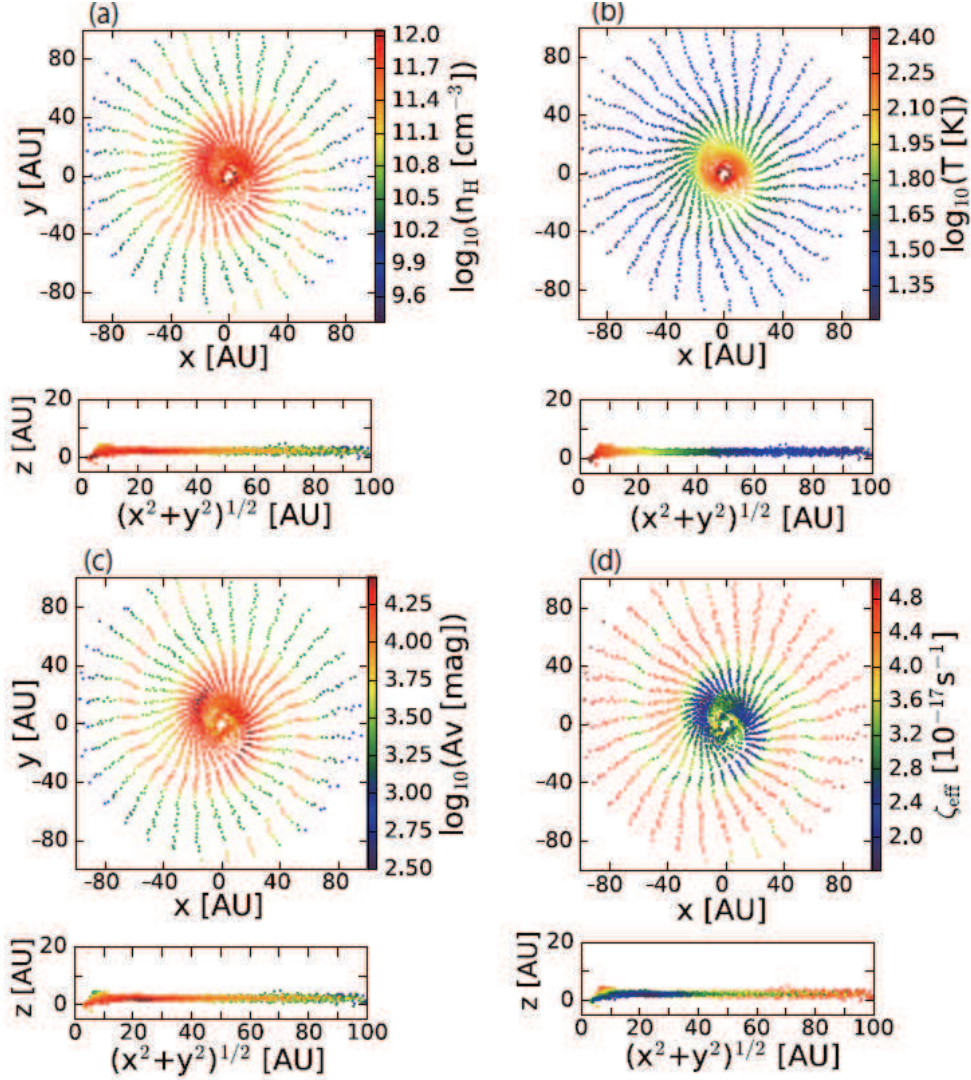


Fig. 2.— Distribution of extracted SPH particles color coded by the number density of hydrogen nuclei (a), temperature (b), the visual extinction (c), and the ionization rate (d) at the final time step of our simulation. The upper panels show the projection onto the $x-y$ plane (i.e. midplane) and the lower panels show the distribution in the radius- z plane. The z -axis corresponds to the rotational axis.

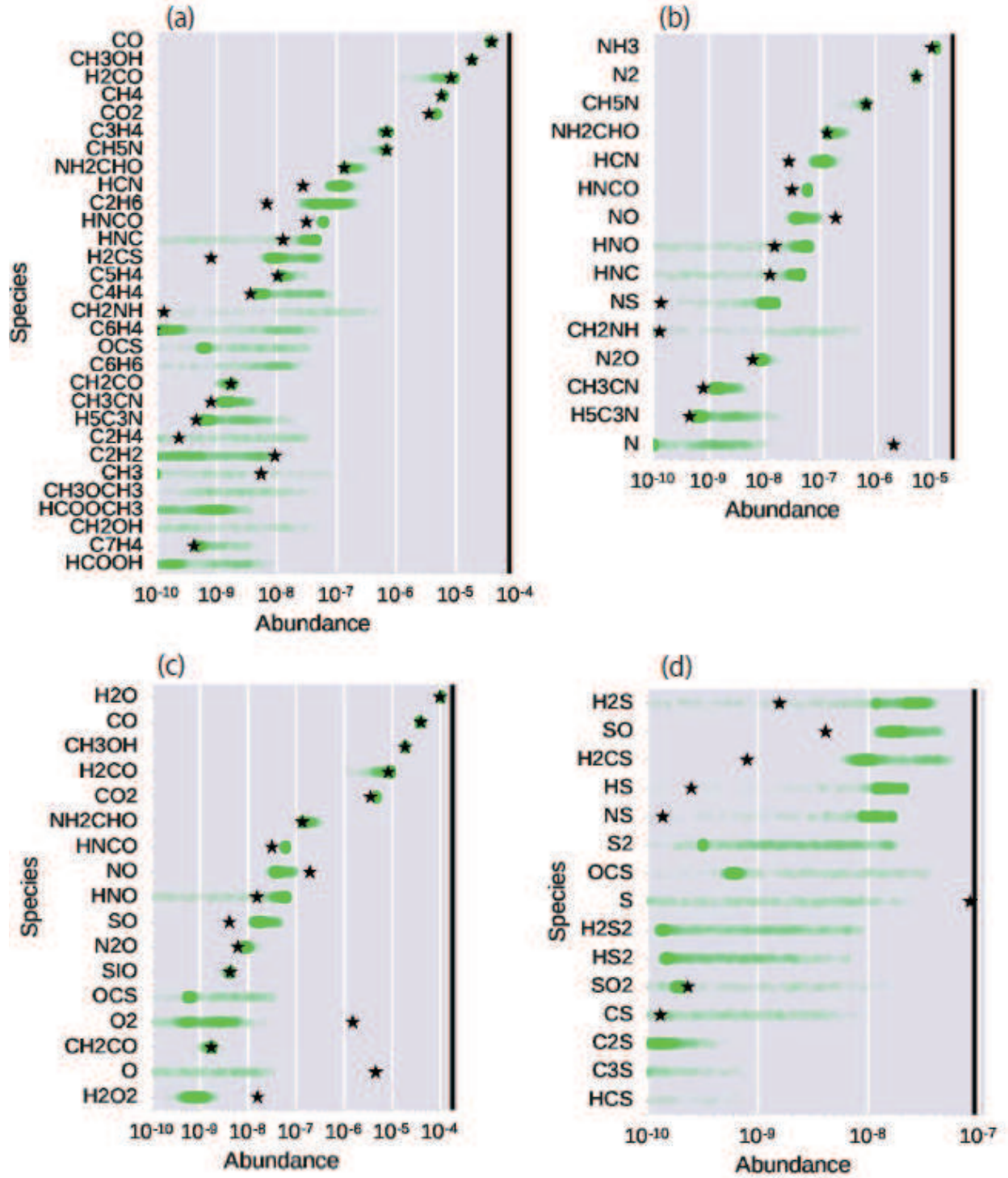


Fig. 3.— Frequency distribution of the total (gas and ice) abundances of the most abundant molecules ($n(i)/n_{\text{H}} \gtrsim 10^{-10}$) at the final time step. The thickness of the green circle is proportional to the number of SPH particles with the corresponding molecular abundances. The star symbols depict the initial abundance.

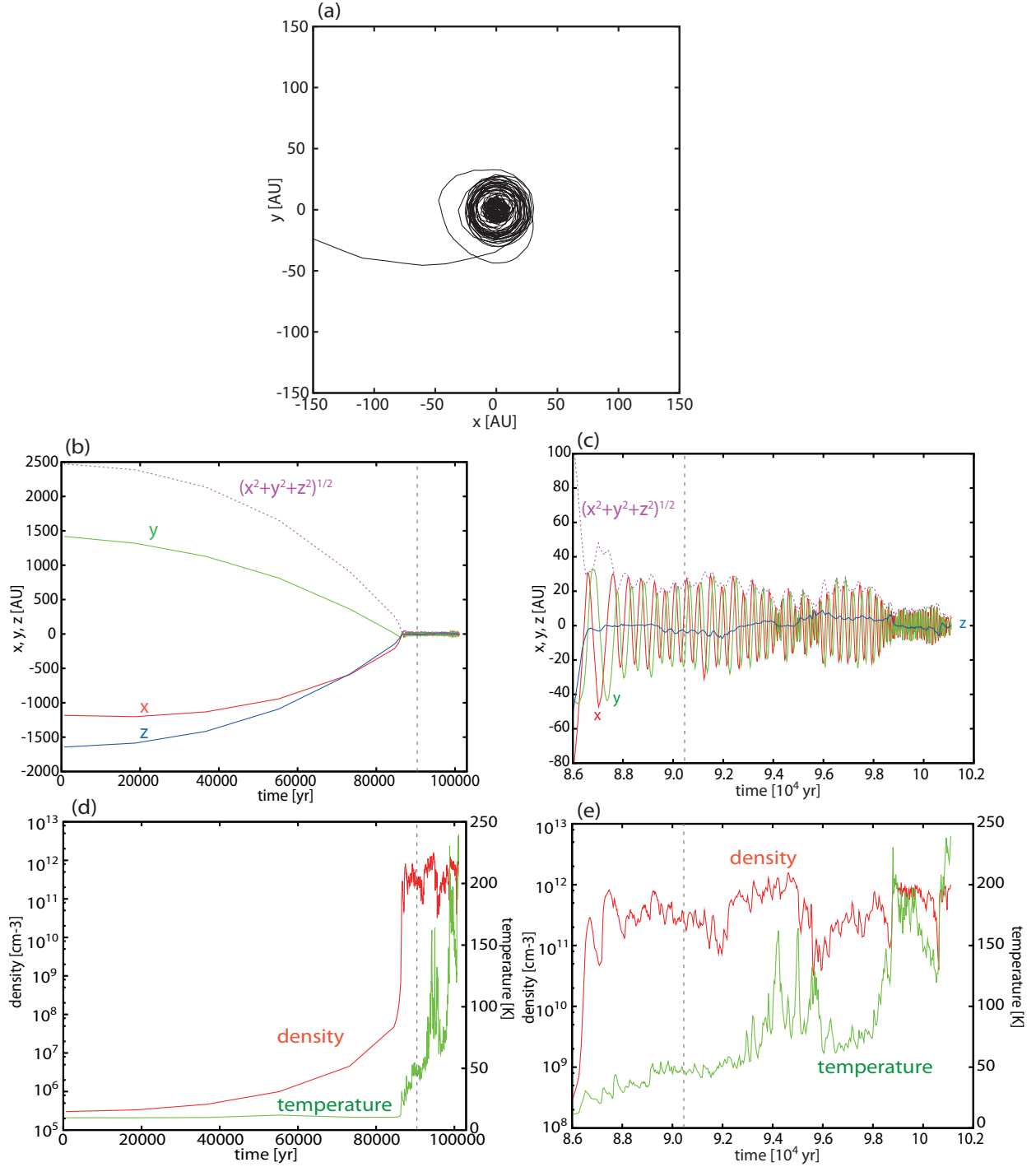


Fig. 4.— Trajectory (a-c) of a SPH particle and the temporal variation of the physical parameters (d-e) in the SPH particle. The protostar is formed at $t = 9.046 \times 10^4$ yr, which is indicated by the gray dashed line.

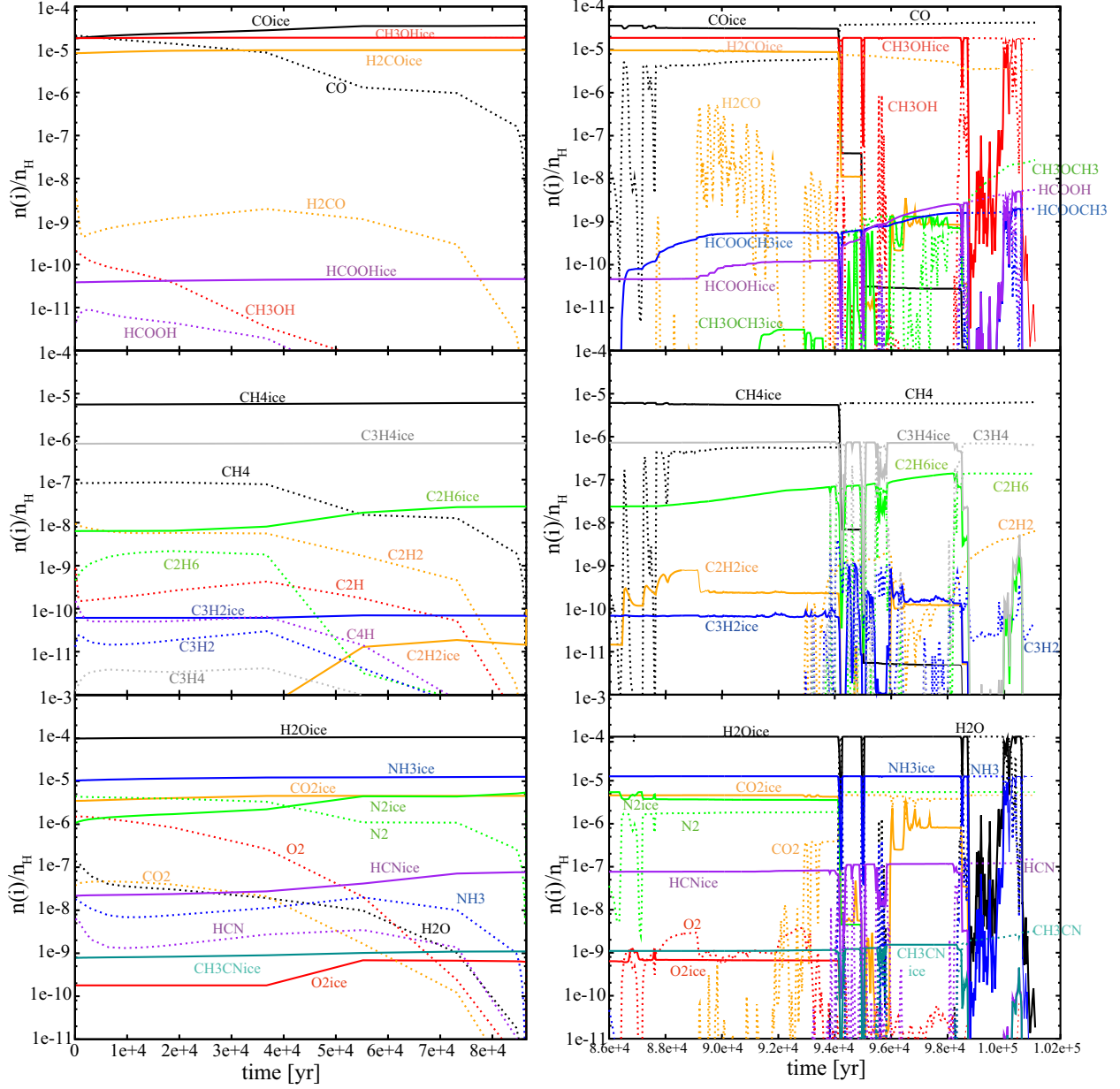


Fig. 5.— Temporal variation of molecular abundances in the SPH particle along the trajectory shown in Figure 4. The left column shows the infalling phase, i.e. $t \leq 8.65 \times 10^4$ yr, while the right column shows the molecular evolution in the forming disk. From top to bottom, the panels show CO and complex organic molecules (COMs), hydrocarbons, O-bearing and N-bearing major molecules, and S-bearing molecules.

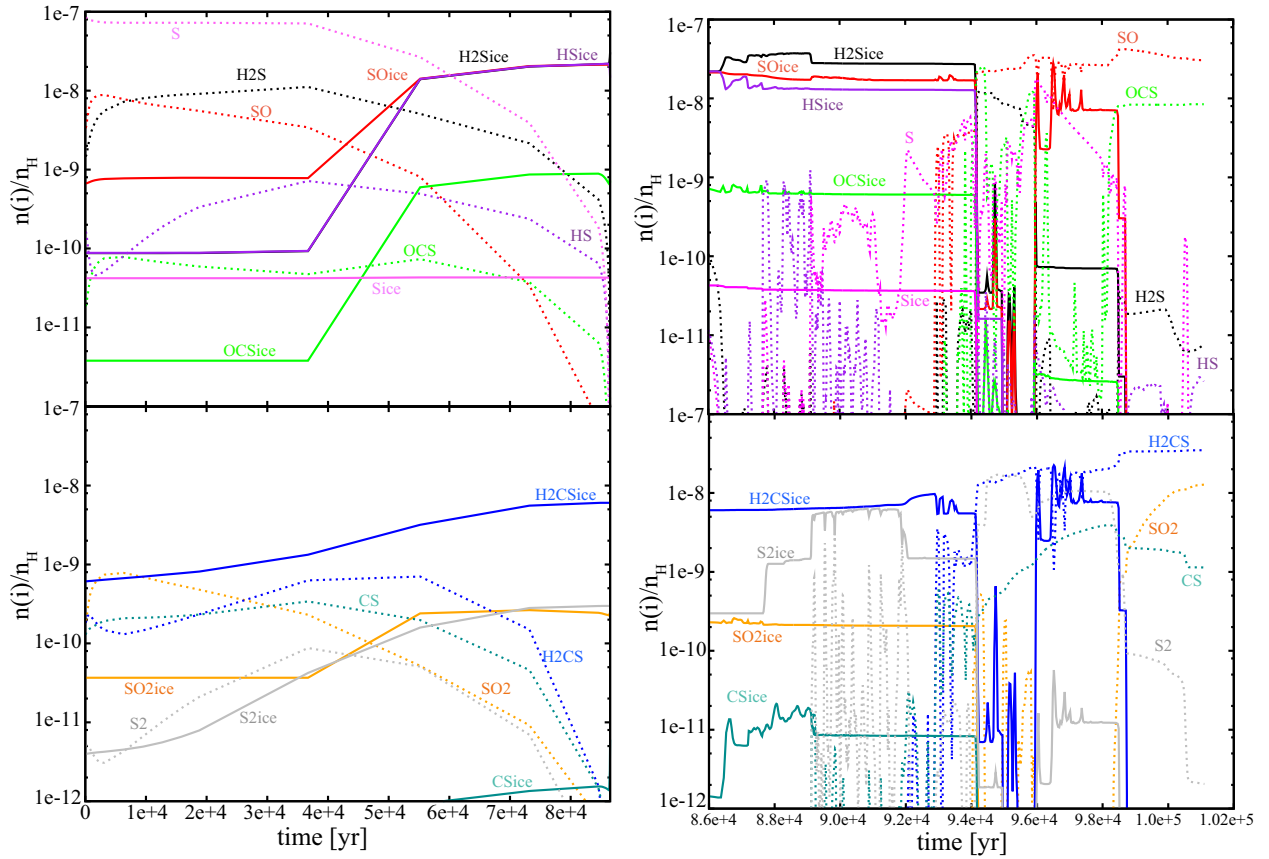


Fig. 5.— cont.

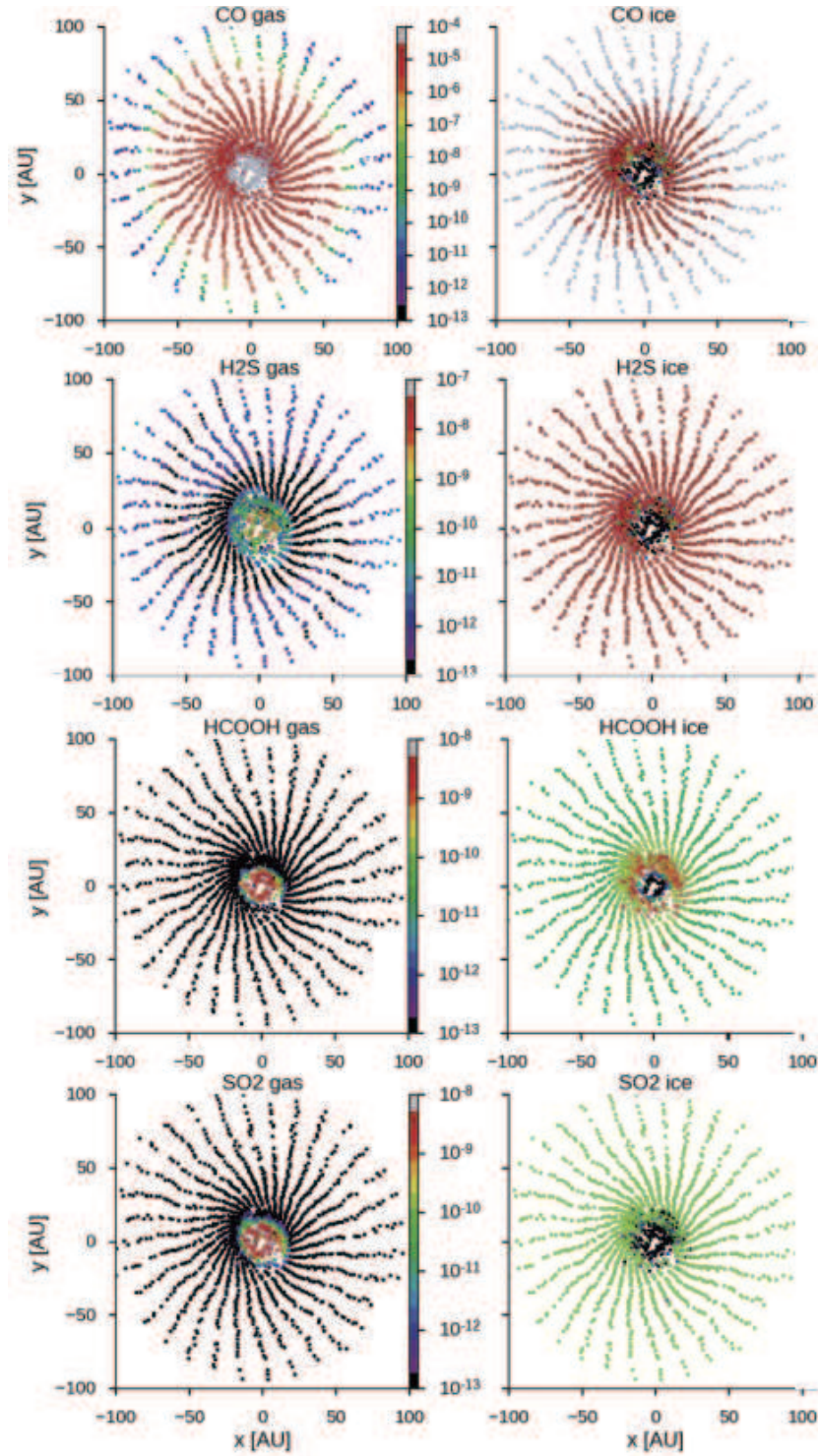


Fig. 6.— Distribution of extracted SPH particles color coded by the molecular abundances at the final time step. CO represents the molecules originate in the cloud core before the onset of collapse. H₂S also originates in the cloud, but is destroyed after sublimation. HCOOH and SO₂ represent the molecules originate in the disk.

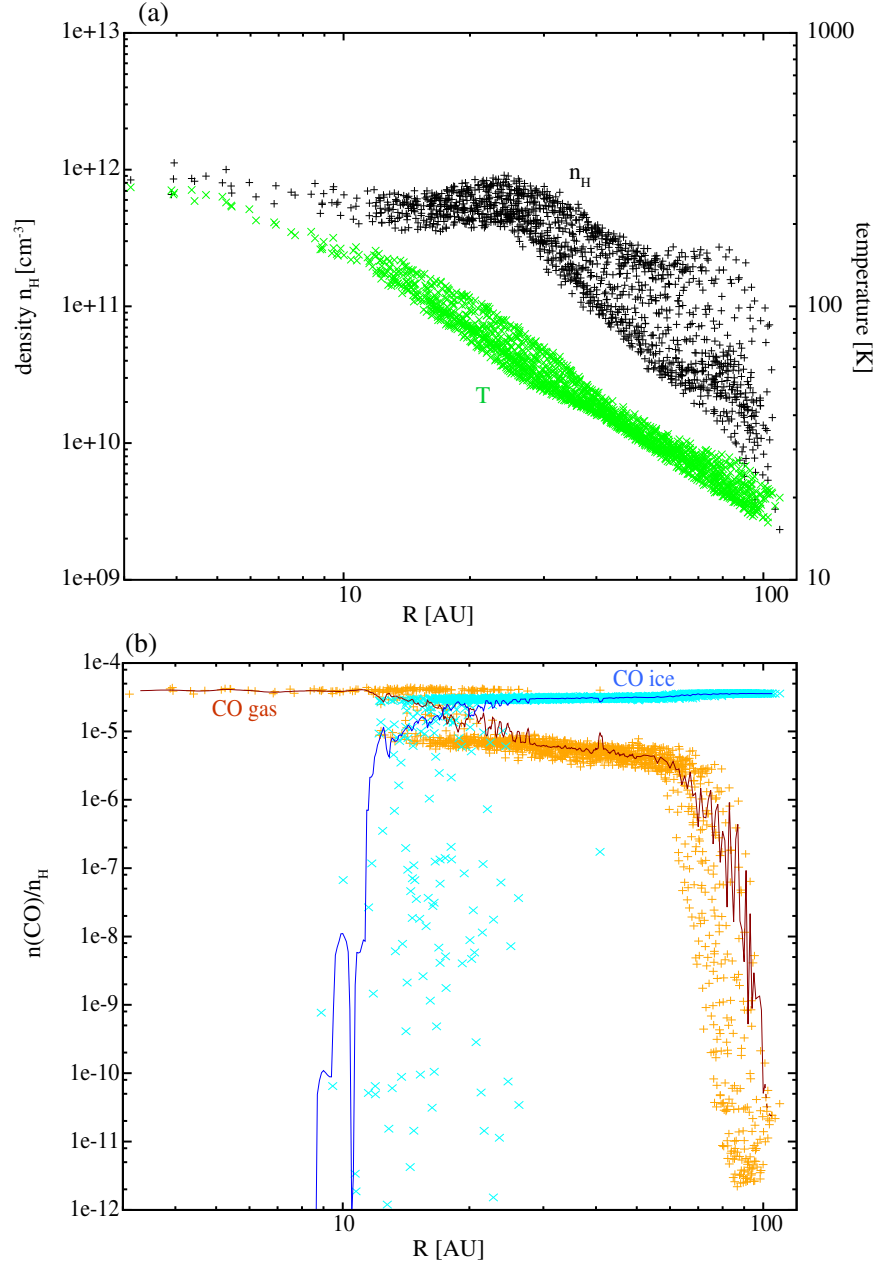


Fig. 7.— Radial distribution of density and temperature (a) and relative abundance of CO to hydrogen nuclei in the gas phase and on grain surfaces (b). The solid lines in panel (b) show the azimuthally averaged abundances.

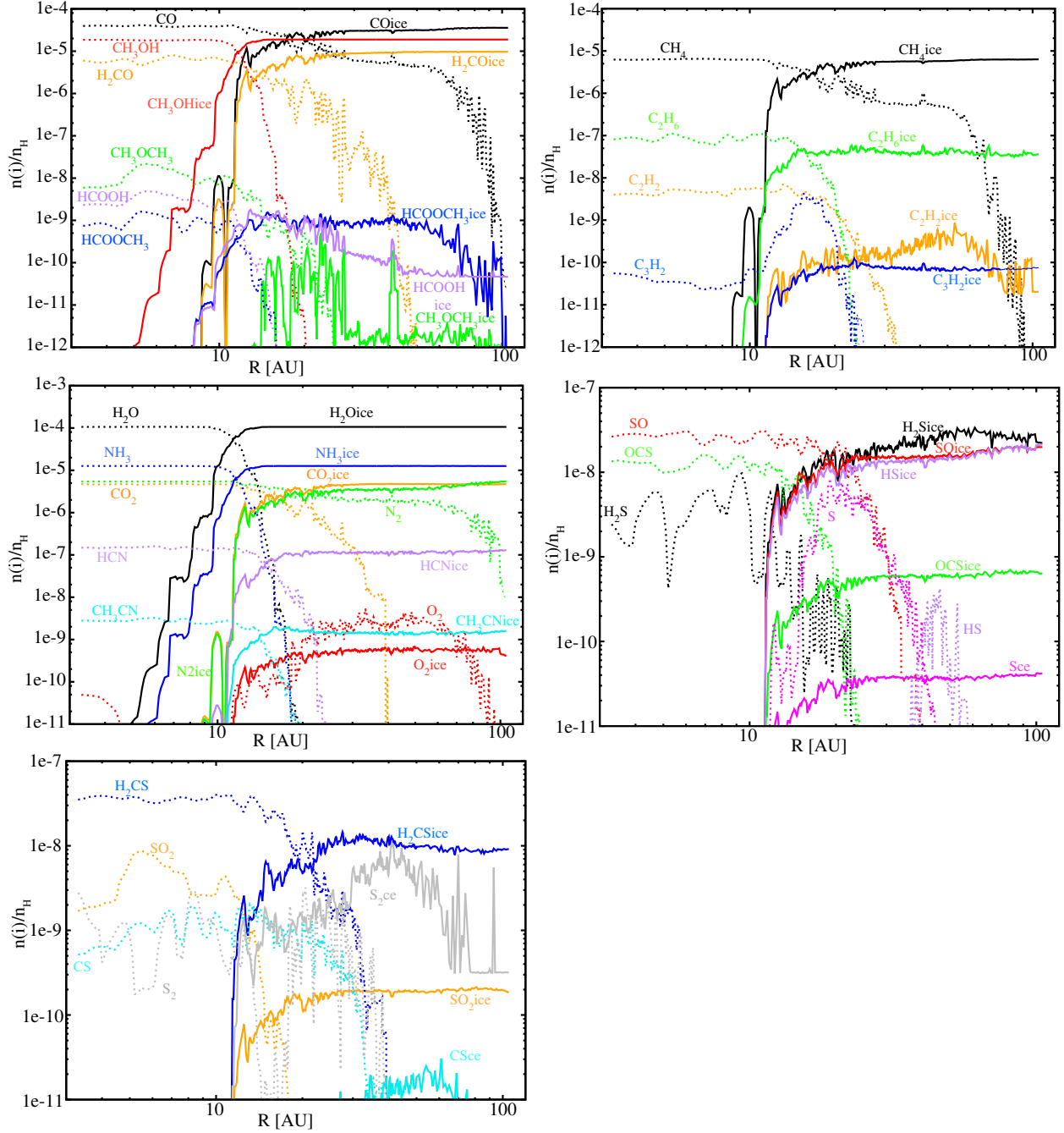


Fig. 8.— Radial distributions of azimuthally averaged molecular abundances.

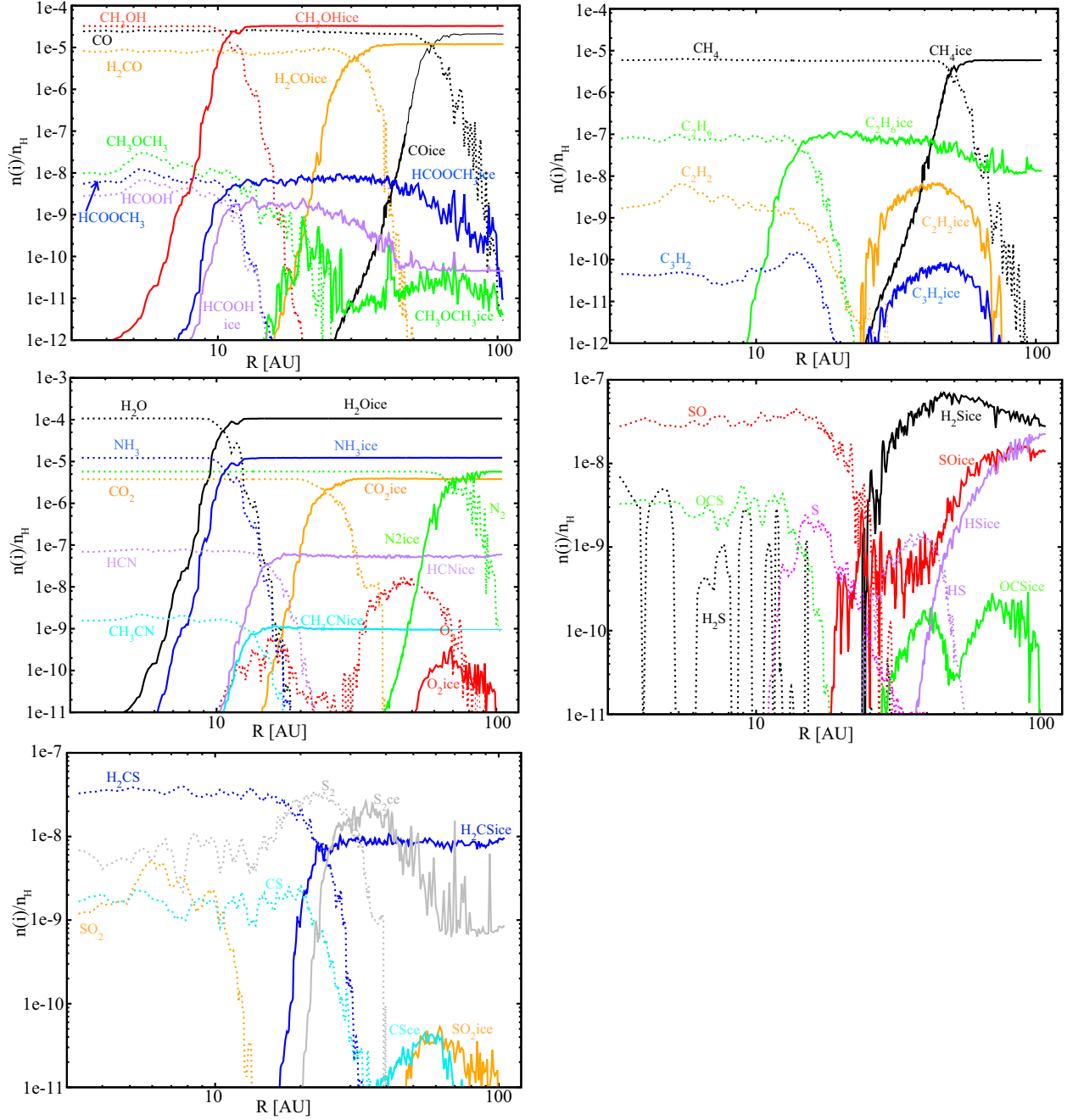


Fig. 9.— Radial distribution of azimuthally averaged molecular abundances as in Figure 8 but for the two-phase model.

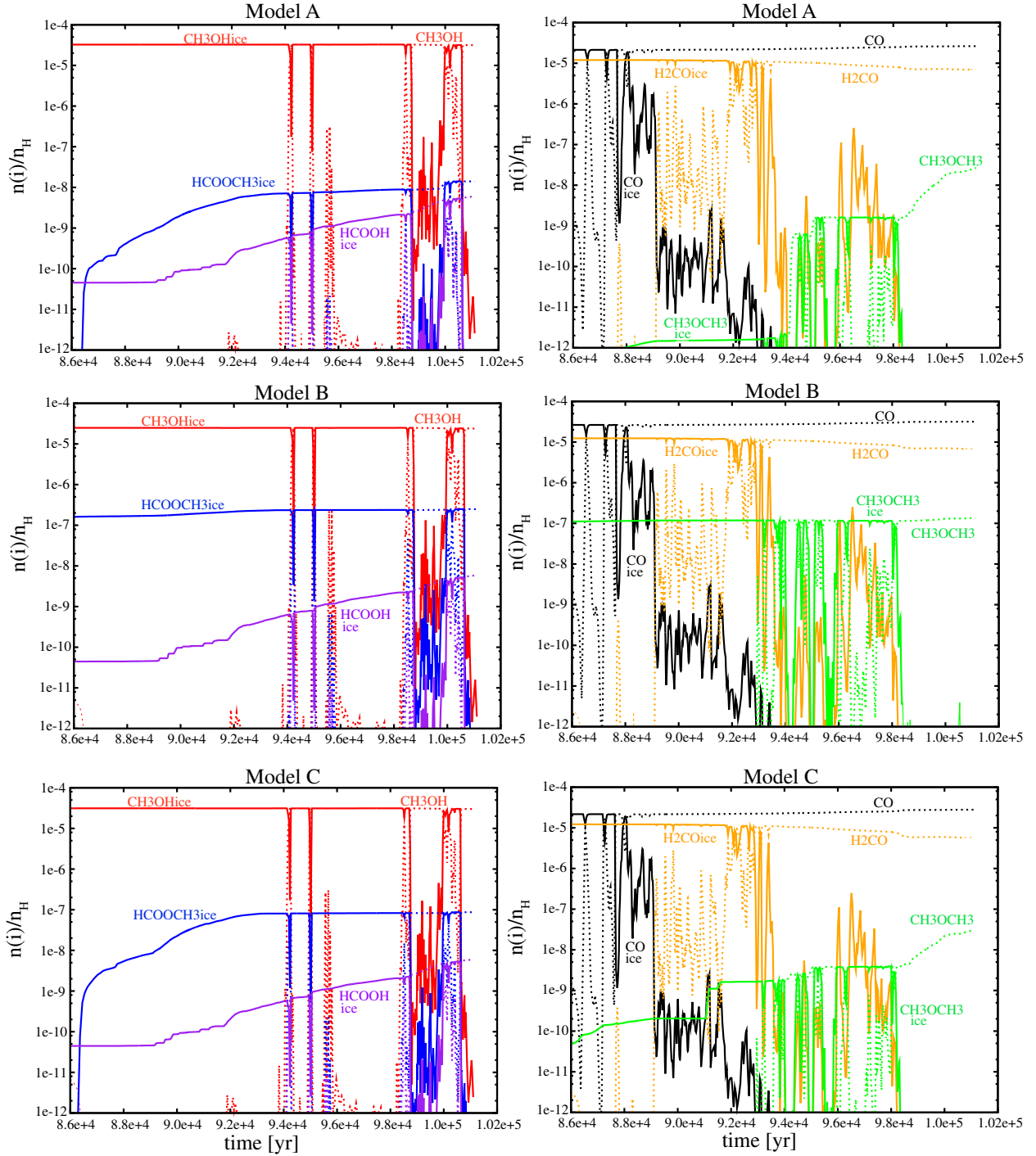


Fig. 10.— Temporal variation of molecular abundances obtained by the two-phase models in the SPH particle along the trajectory shown in Figure 4. The upper, middle, and the bottom panels show Model A, B, and C, respectively.